44th AIAA Aerospace Sciences Meeting and Exhibit, 9-12 January 2006, Reno, Nevada

Accurate Estimates of Fine Scale Reaction Zone Thicknesses in Hydrocarbon Detonations

Joseph M. Powers* and Samuel Paolucci†

University of Notre Dame, Notre Dame, Indiana, 46556-5637, USA

Fully resolved predictions of steady, one-dimensional detonations near the Chapman-Jouguet state in mixtures of methane-air and methane-oxygen-argon are presented. The model is restricted to inviscid continuum mixtures of calorically imperfect ideal gases described by detailed Arrhenius kinetics. Consistent with estimates from an underlying molecular collision theory, an eigenvalue analysis of locally linearized equations reveals that the continuum theory predicts evolution of species mass fractions on scales as fine as 10^{-5} cm, the mean free path length scale. In that such scales are orders of magnitude smaller than most discretization scales employed in simulations of combustion in engineering devices, it is suggested that one potential explanation for existing discrepancies between numerical prediction and observed data is that the calculations are highly under-resolved.

I. Introduction

Computational simulation of compressible reactive flow utilizing detailed kinetic mechanisms pervades the modern aerospace engineering literature and is endemic in industry. Detailed kinetics enable the robust capture of a variety of physical phenomena ranging from ignition delay events to pollution formation as well as any phenomena in which the dynamically evolving physical properties of a multi-component mixture play an important role. And despite great advances in hardware and software, great challenges remain.[1] Many of these challenges are directly related to the multi-scale nature of the flow and the difficulty in computing solutions which resolve all physically relevant scales intrinsic to the underlying mathematical model.[2] For example, a recent exercise[3] in which several computational algorithms were employed in an effort to reproduce results of a benchmark experiment of a ram accelerator generated, according to the authors, "widely different outcomes," with strong sensitivity to induction zone dynamics. Another recent study[4] which included both computational predictions and observations of pulse detonation engines concluded that the important run-up distance to detonation to be "underpredicted" and that "simulation of the DDT [deflagration to detonation transition] process remains a challenge." Such issues, of course, transcend reactive gas dynamics; analogous difficulties in related fields are easily found. For example, Kadanoff[5] summarizes some notable recent failures in computational simulations of sonoluminescence, Rayleigh-Taylor instability, and wave breaking. He concludes that "resolution matters."

This paper poses and answers a focused, critical question in multi-scale one-dimensional steady reactive flow of methane-based mixtures: what is the minimum length scale which must be resolved in order for the mathematical problem to be verified.[6–7] This work is a direct extension of the authors' recent study[8] of length scales in $H_2/O_2/N_2$ detonation. It further draws upon an upcoming review[2] to summarize some more general concepts. That such a question is important is explicitly recognized by the AIAA, which states,[9] "The AIAA journals will not accept for publication any paper reporting (1) numerical solutions of an engineering problem that fails adequately to address the accuracy of the computed results..." In explaining this policy, it is noted, "The accuracy of the computed results is concerned with how well the specified governing equations in the paper have been solved numerically. The appropriateness of the governing equations for modeling the physical phenomena and comparison with experimental data is not part of this evaluation."

*Associate Professor, Department of Aerospace and Mechanical Engineering, AIAA Associate Fellow, powers@nd.edu.

†Professor, Department of Aerospace and Mechanical Engineering, paolucci@nd.edu.

The key new conclusion is that, in the same way that $H_2/O_2/N_2$ continuum detonation simulations with detailed kinetics demand grid resolutions near 10^{-5} cm, so also do simulations of $CH_4/O_2/N_2/Ar$ mixtures. An analysis is given to demonstrate that such fine length scales predicted by continuum theory are fully consistent with the averaged predictions of the underlying molecular collision theory.

To guarantee that the new results for methane detonation length scales are fully reproducible, the model and parameters are presented in great detail. This is in response to many deficiencies in the existing literature: it is an unfortunate practice that many authors omit, or render opaque, critical details in their published work to the extent that their results are irreproducible by others. In fact, in response to such endemic shortcomings, the program chairmen of the upcoming 31^{st} International Combustion Symposium recently entreated all referees to suggest appropriate remedies, stating [a] "If the mechanisms are not openly available (now and into the future), the scientific basis of the paper is questionable, in that it is not possible for other researchers to verify or refute the conclusions drawn."

The paper is organized as follows. First, the model equations are presented in a fashion similar to that of Ref. 8. Next, the detailed kinetic model of Yungster and Rabinowitz,[10] a reduction of the model given by Frenklach,[11] is presented. For minor software-compatibility reasons, the three reactions with pressure-dependent rates from Ref. 10 were replaced by their equivalent from GRI 3.0.[12] A brief description is given of how the reactive flow model is reduced and length scales are determined through local linear analysis of the system's spatial eigenvalues. The kinetic model is then mathematically verified against predictions given by Petersen and Hanson[13] and validated in a limited sense against experimental observations of Spadaccini and Colket[14] and Tieszen, et al.[15] As recently noted,[16] full experimental validation of methane kinetic models under a broad range of conditions remains a challenge, but this issue is not considered here. Next, detailed results, qualitatively similar to those of Ref. 8, for a detonation near the Chapman-Jouguet (CJ) state in a stoichiometric methane-air mixture initially at standard atmospheric conditions are given, and minimum length scales are presented. These scales are compared to predictions of a simplified molecular theory, and comments are given on why the continuum theory is appropriate to use at and above these scales. Modern published unsteady and multi-dimensional steady simulations of methane-based detonation with detailed kinetics [10,17–20] are examined and found to be severely under-resolved. The paper is closed with brief conclusions.

II. Mathematical Model

A. Governing Equations

The set of model equations, equivalent to those of Ref. 8, is given next. Detailed explanations of their physical justification are given in a variety of sources, cf. Kuo[21] or Kee, et al.[22]

1. Fundamental Evolutionary Equations

The following equations, written in unsteady conservative form, describe the behavior of a one-dimensional inviscid mixture of N gaseous molecular species composed of L atomic elements which undergo J reactions:

$$\frac{\partial \rho}{\partial t} + \frac{\partial}{\partial x}(\rho u) = 0, \tag{1}$$

$$\frac{\partial}{\partial t}(\rho u) + \frac{\partial}{\partial x}\left(\rho u^2 + p\right) = 0, \tag{2}$$

$$\frac{\partial}{\partial t}\left(\rho\left(e + \frac{u^2}{2}\right)\right) + \frac{\partial}{\partial x}\left(\rho u\left(e + \frac{u^2}{2} + \frac{p}{\rho}\right)\right) = 0, \tag{3}$$

$$\frac{\partial}{\partial t}(\rho Y_i) + \frac{\partial}{\partial x}(\rho u Y_i) = \dot{\omega}_i \mathcal{M}_i, \qquad (i = 1, \ldots, N-1). \tag{4}$$

The independent variables are the distance coordinate, x, and time, t. The dependent variables are density ρ, velocity u, pressure p, specific internal energy e, species mass fraction $Y_i, i = 1, \ldots, N-1$, and molar production rate per unit volume for specie i, $\dot{\omega}_i, i = 1, \ldots, N-1$. The parameters are the molar mass of molecular specie i, $\mathcal{M}_i, i = 1, \ldots N-1$. Equations (1-3) describe the conservation of mixture mass, linear momentum, and energy, respectively. Equations (4) describe the evolution of $N-1$ molecular species mass fractions.

[a] Alden, M., and Pope, S. B., private communication, December 2005.

2. Algebraic Constitutive Models

The system is completed by the following algebraic equations:

$$p = \rho \Re T \sum_{i=1}^{N} \frac{Y_i}{\mathcal{M}_i}, \tag{5}$$

$$e = \sum_{i=1}^{N} Y_i \left(h_i^o - \frac{\Re T}{\mathcal{M}_i} \right), \tag{6}$$

$$1 = \sum_{i=1}^{N} Y_i, \tag{7}$$

$$\dot{\omega}_i = \sum_{j=1}^{J} \nu_{ij} r_j, \qquad (i = 1, \ldots, N-1), \tag{8}$$

$$r_j = k_j \left(\underbrace{\prod_{k=1}^{N} \left(\frac{\rho Y_k}{\mathcal{M}_k} \right)^{\nu'_{kj}}}_{\text{forward}} - \underbrace{\frac{1}{K_j^c} \prod_{k=1}^{N} \left(\frac{\rho Y_k}{\mathcal{M}_k} \right)^{\nu''_{kj}}}_{\text{reverse}} \right), \quad (j = 1, \ldots, J), \tag{9}$$

$$k_j = A_j T^{\beta_j} \exp\left(-\frac{\Theta_j}{T} \right), \qquad (j = 1, \ldots, J), \tag{10}$$

$$K_j^c = \left(\frac{p^{ref}}{\Re T} \right)^{\sum_{m=1}^{N} \nu_{mj}} \exp\left(-\frac{\sum_{m=1}^{N} \overline{\mu}_m^o \nu_{mj}}{\Re T} \right), \qquad (j = 1, \ldots, J), \tag{11}$$

$$c_{pi} = \frac{\Re}{\mathcal{M}_i} \left(a_{1i} + a_{2i} T + a_{3i} T^2 + a_{4i} T^3 + a_{5i} T^4 \right), \qquad (i = 1, \ldots, N), \tag{12}$$

$$h_i^o = h_i^{ref} + \int_{T^{ref}}^{T} c_{pi} \, d\hat{T}, \qquad (i = 1, \ldots, N), \tag{13}$$

$$s_i^o = s_i^{ref} + \int_{T^{ref}}^{T} \frac{c_{pi}}{\hat{T}} \, d\hat{T}, \qquad (i = 1, \ldots, N), \tag{14}$$

$$\overline{\mu}_i^o = \mathcal{M}_i \left(h_i^o - T s_i^o \right), \qquad (i = 1, \ldots, N), \tag{15}$$

$$\mathcal{M}_i = \sum_{l=1}^{L} m_l \phi_{li}, \qquad (i = 1, \ldots, N), \tag{16}$$

$$0 = \sum_{i=1}^{N} \phi_{li} \nu_{ij}, \qquad (j = 1, \ldots, J), \ (l = 1, \ldots, L), \tag{17}$$

$$\nu_{ij} = \nu''_{ij} - \nu'_{ij}, \qquad (i = 1, \ldots, N), \ (j = 1, \ldots, J). \tag{18}$$

New dependent variables are the temperature T, specific heat at constant pressure of the i^{th} specie c_{pi}, mass fraction of the N^{th} specie Y_N, reaction rate of the j^{th} reaction r_j, temperature-dependent Arrhenius coefficient for the j^{th} reaction k_j, and so-called equilibrium "constant" of the j^{th} reaction K_j^c. Also, a set of new variables for the i^{th} specie, denoted with a superscript "o" to indicate evaluation at the reference pressure, are defined as the chemical potential per unit mole, enthalpy per unit mass, and entropy per unit mass, $\overline{\mu}_i^o$, h_i^o, and s_i^o, respectively. The bar notation indicates a per mole basis, and $\hat{T}$ is a dummy variable of integration.

Parameters in Eqs. (5-18) are as follows. The universal gas constant is $\Re = 8.314 \times 10^7 \; erg/mole/K$. The pressure and temperature at the reference state are $p^{ref} = 1 \; atm$ and $T^{ref} = 298 \; K$, respectively. For each molecular specie from $i = 1, \ldots, N$, one has reference state specific enthalpy and entropy, h_i^{ref}, s_i^{ref}. For each reaction $j = 1, \ldots, J$, one has collision frequency factor A_j, exponent characterizing power-law temperature dependency β_j, activation temperature Θ_j, and stoichiometric coefficients denoting the number of moles of reactant and product, respectively, of specie i in reaction j, ν'_{ij}, ν''_{ij}, as well as the net stoichiometric coefficients ν_{ij}. The parameters $a_{1i}, \ldots, a_{5i}$ are coefficients in a fourth order polynomial curve fit for c_{pi}. For

$l = 1, \ldots, L$, the molar mass of element l is m_l. For specie $i = 1, \ldots, N$, and atomic element $l = 1, \ldots, L$, the species atomic element index giving number of moles of atomic element l in specie i is ϕ_{li}.

Equation (5) is a thermal equation of state for a mixture of ideal gases which obeys Dalton's law. Equation (6) is the corresponding caloric equation of state. Equation (7) constrains the species mass fractions to sum to unity. Equation (8) is an expression for the molar species evolution rate per unit volume for specie i. Equation (9) is an expression of the law of mass action for reaction j constructed so as to insure the forward and reverse reaction rate components satisfy Le Châtlier's principle as each individual reaction approaches equilibrium. Equation (10) defines the temperature-dependent Arrhenius rate coefficient. Equation (11) is an equation for the equilibrium "constant" for each reaction; actually K_j^c is a function of T. Equation (12) is the fourth order polynomial curve fit for c_{pi}. Equations (13-15) define the enthalpy, entropy, and chemical potential of specie i, evaluated at p^{ref}, as functions of temperature. Equation (16) defines the molar mass of molecular specie i in terms of its constitutive atomic elements. Equation (17) is a stoichiometric constraint on atomic element l in reaction j which represents an atomic mass balance for each atom. Finally, Eq. (18) defines the net stoichiometric coefficients.

3. Pressure-Dependent Reaction Rates

A small number of reaction rates can exhibit pressure-dependency and are known as "fall-off" reactions. For such reactions, Eq. (10) is not used to calculate k_j; instead, the convoluted procedure described fully in a variety of sources[21,22] is employed and summarized here.

At high pressures, one set of values for A_j, Θ_j, and β_j are adopted and labeled A_j^∞, Θ_j^∞, and β_j^∞. Using Eq. (10), these yield the Arrhenius coefficient

$$k_j^\infty = A_j^\infty T^{\beta_j^\infty} \exp\left(-\frac{\Theta_j^\infty}{T}\right). \tag{19}$$

Such reactions are typically independent of the molar concentration of a third body, denoted by $[M]$. At low pressures, the reaction rates come to depend on $[M]$, and a second set of kinetic coefficients is utilized, namely A_j^0, Θ_j^0, and β_j^0, which define the low pressure Arrhenius coefficient

$$k_j^0 = A_j^0 T^{\beta_j^0} \exp\left(-\frac{\Theta_j^0}{T}\right). \tag{20}$$

The actual k_j used in the calculation is an interpolation between k_j^∞ and k_j^0. While a variety of interpolation protocols can be employed, here the Troe method[23] is used. This method requires the following steps. First, define $[M]$ as

$$[M] = \rho \sum_{i=1}^{N} \eta_i \frac{Y_i}{\mathcal{M}_i}. \tag{21}$$

Here, η_i is an empirically determined dimensionless collision efficiency parameter. Unless otherwise specified, $\eta_i = 1$. Next, define the dimensionless so-called "reduced pressure," p_j^r, as

$$p_j^r = \frac{k_j^0 [M]}{k_j^\infty}. \tag{22}$$

In addition, define the temperature-dependent dimensionless variable F_j^{cent} as

$$F_j^{cent} = (1 - \alpha_j) \exp\left(-\frac{T}{T_j^{***}}\right) + \alpha_j \exp\left(-\frac{T}{T_j^*}\right) + \exp\left(-\frac{T_j^{**}}{T}\right). \tag{23}$$

Here, α_j, T_j^{***}, T_j^*, and T_j^{**} are constants fixed for each reaction; α_j is dimensionless, while the other three parameters have units of K. Then, define the intermediate temperature-dependent dimensionless variables c_j and n_j, and constant d as

$$c_j = -0.4 - 0.67 \log_{10} F_j^{cent}, \tag{24}$$

$$n_j = -0.75 - 1.27 \log_{10} F_j^{cent}, \tag{25}$$

$$d = 0.14. \tag{26}$$

Next, one calculates the new dimensionless variable F_j from

$$\log_{10} F_j = \left\{ \left[1 + \left(\frac{\log_{10} p_j^r + c_j}{n_j - d\left(\log_{10} p_j^r + c_j\right)} \right)^2 \right]^{-1} \right\} \left(\log_{10} F_j^{cent}\right). \tag{27}$$

Finally, knowing F_j, one calculates the interpolated Arrhenius rate coefficient to be

$$k_j = k_j^{\infty} \left(\frac{p_j^r}{1 + p_j^r} \right) F_j. \tag{28}$$

Note that because of the ambiguity of the "log" operator, which is found in most sources, e.g. Ref. 21, some sources, e.g. Ref. 13, incorrectly interpret the operator to be a natural logarithm instead of a base ten logarithm, as explicated by Ref. 22 and the actual FORTRAN source code.[24]

4. Complete System

After use of Eqs. (8-28) to eliminate $\dot{\omega}_i$ in Eq. (4), Eqs. (1-7) form $5+N$ equations in the $5+N$ unknowns, ρ, u, p, e, T, $Y_1, \ldots, Y_N$.

5. Auxiliary Equations

Additional useful auxiliary equations are as follows:

$$c_{vi} = c_{pi} - \frac{\Re}{\mathcal{M}_i}, \qquad (i = 1, \ldots, N), \tag{29}$$

$$c_p = \sum_{i=1}^{N} Y_i c_{pi}, \tag{30}$$

$$c_v = \sum_{i=1}^{N} Y_i c_{vi}, \tag{31}$$

$$\gamma = \frac{c_p}{c_v}, \tag{32}$$

$$c = \sqrt{\gamma \frac{p}{\rho}}, \tag{33}$$

$$\mathsf{M} = \frac{u}{c}, \tag{34}$$

$$h_i^o = \frac{\Re}{\mathcal{M}_i} \left(a_{1i} T + \frac{1}{2} a_{2i} T^2 + \frac{1}{3} a_{3i} T^3 + \frac{1}{4} a_{4i} T^4 + \frac{1}{5} a_{5i} T^5 + a_{6i} \right), \qquad (i = 1, \ldots, N), \tag{35}$$

$$h_i^{ref} = \frac{\Re}{\mathcal{M}_i} \left(a_{1i} T^{ref} + \frac{1}{2} a_{2i} \left(T^{ref}\right)^2 + \frac{1}{3} a_{3i} \left(T^{ref}\right)^3 + \frac{1}{4} a_{4i} \left(T^{ref}\right)^4 + \frac{1}{5} a_{5i} \left(T^{ref}\right)^5 + a_{6i} \right), \ (i = 1, \ldots, N), \tag{36}$$

$$s_i^o = \frac{\Re}{\mathcal{M}_i} \left(a_{1i} \ln T + a_{2i} T + \frac{1}{2} a_{3i} T^2 + \frac{1}{3} a_{4i} T^3 + \frac{1}{4} a_{5i} T^4 + a_{7i} \right), \qquad (i = 1, \ldots, N), \tag{37}$$

$$s_i^{ref} = \frac{\Re}{\mathcal{M}_i} \left(a_{1i} \ln\left(T^{ref}\right) + a_{2i} \left(T^{ref}\right) + \frac{1}{2} a_{3i} \left(T^{ref}\right)^2 + \frac{1}{3} a_{4i} \left(T^{ref}\right)^3 + \frac{1}{4} a_{5i} \left(T^{ref}\right)^4 + a_{7i} \right), \ (i = 1, \ldots, N). \tag{38}$$

New dependent variables in Eqs. (29-38) are as follows. For each molecular specie, $i = 1, \ldots, N$, one has the specific heat at constant volume, c_{vi}. One also has the mass-averaged specific heats at constant pressure and volume, respectively, c_p, c_v, the ratio of specific heats for the mixture, γ, the frozen acoustic speed, c, and the Mach number, M. New parameters are a_{6i}, a constant in the definition of h_i^o, and a_{7i}, a constant in the definition of s_i^o. Equations (29-34) are definitions of c_{vi}, c_p, c_v, γ, c, and M, respectively. Equations (35) and (37) are consequences of applying Eq. (12) to Eqs. (13) and (14). The constants h_i^{ref} and a_{6i} are

related through Eq. (36). Likewise, s_i^{ref} and a_{7i} must satisfy Eq. (38). As a relic of the form chosen for the polynomial curve fit, one must tolerate a clumsy form in which terms with the "units" of logarithm of temperature appear in Eqs. (38); proper selection of a_{7i} from Eq. (38) guarantees cancellation of such terms.

B. Reduction to Standard Dynamic Systems Form

It is shown in detail in Ref. 8 how this system can be reduced significantly. In short, one first employs conservation of atomic elements and uses the fact that only mixtures which are initially spatially homogeneous are being considered. This allows one to integrate L differential equations to form L algebraic constraints. Next, one assumes that a steady state solution exists in a reference frame traveling at velocity D. In this frame, the partial differential equations reduce to ordinary differential equations (ODEs), and the mass, momentum, and energy equations can be explicitly integrated to form three additional algebraic equations, which are extensions of the well-known Rankine-Hugoniot jump conditions. The extensions are actually valid both over a shock jump as well as throughout the reaction zone structure. The solutions are double valued, and care must be used to distinguish the subsonic and supersonic branches. Here, primary concern for the flow past the shock is with the subsonic branch. Combination of the element conservation equations, the extended Rankine-Hugoniot equations, and the thermodynamic state equations with the remaining ODEs allows the system to be written in the standard dynamical systems form

$$\frac{dY_i}{dx} = f_i(Y_i, \ldots, Y_{N-L}), \qquad Y_i(0) = Y_{io}, \qquad (i = 1, \ldots, N-L), \tag{39}$$

where f_i is a non-linear function of the dependent variables given by $f_i = \dot{\omega}_i \mathcal{M}_i/(\rho_o D),\ (i = 1, \ldots, N-L)$. As a subscript, "o" denotes an unshocked ambient value. Equation (39) can be solved by a variety of well known numerical methods to obtain $Y_i(x),\ (i = 1, \ldots, N-L)$. Subsequently, because all secondary variables, such as p, T, and u, are available as algebraic functions of $Y_i,\ (i = 1, \ldots, N-L)$, they can also be found as functions of x.

To correlate the position in the reaction zone with the time elapsed since a Lagrangian fluid particle has traversed the shock, one can integrate the fluid particle velocity definition, $u = dx/dt$, to form

$$t = \int_0^x \frac{d\hat{x}}{u(\hat{x})}. \tag{40}$$

Here $\hat{x}$ is a dummy variable of integration, and $x = 0$ is aligned with the shock wave, which is stationary in this reference frame. This calculation is useful in obtaining the ignition delay time, t_{ign}, commonly measured in shock tube experiments. One can also estimate t_{ign} by reformulating Eqs. (1-18) into a spatially homogeneous isobaric time-dependent system and then solving an alternate system of time-dependent ODEs. Both methods yield essentially identical results.

C. Length Scale Estimation

It is shown in detail in Ref. 8 how the local length scales can be estimated. One first finds the Jacobian $\mathbf{J}$, defined by

$$\mathbf{J} \equiv \left.\frac{\partial f_i}{\partial Y_j}\right|_{Y_k,\ k \neq j}, \qquad (i = 1, \ldots, N-L;\ j = 1, \ldots, N-L;\ k = 1, \ldots, N-L). \tag{41}$$

When evaluated at a given spatial point, $\mathbf{J}$ is a constant matrix. It has a set of $N-L$ eigenvalues, $\lambda_i,\ (i = 1, \ldots, N-L)$, and the amplitude of a given local eigenmode will have significant variation over a length scale ℓ_i defined by

$$\ell_i \equiv \frac{1}{|\mathrm{Re}(\lambda_i)|}, \qquad (i = 1, \ldots, N-L). \tag{42}$$

Should the eigenvalues come in complex conjugate pairs, their eigenmodes will have amplitudes evolving on the same length scale, and a new oscillatory length scale will appear. While this oscillatory length scale is not difficult to consider, nearly all the eigenvalues in this study are real, as well as negative, and so no special consideration will be given to the complex case here.

III. Computational Method

All calculations were performed on a single processor Hewlett-Packard Linux desktop computer with an approximate speed of around 1 GHz. Typical calculations, done in double precision, were completed within three minutes. A FORTRAN 90 code that drew upon standard International Mathematical and Statistical Libraries (IMSL) routines DNEQNF for Newton iteration, DFDJAC for Jacobian evaluation, and DEVLRG for eigenvalue computation was used. For evaluation of thermochemical properties and kinetic rates, subroutines available in a double precision version of the public domain edition of the CHEMKIN[24] package were utilized; no other general CHEMKIN tools for solving specific physical problems were employed. Using a well documented method,[25] this package draws upon a standard thermodynamic data base[12] which contains properties for a wide variety of constituents; these include coefficients for polynomial curve fits for the variation of specific heats with temperature as well as constants which can be correlated with reference state values of species enthalpy and entropy.

For numerical integration, an implicit Adams method with functional iteration as embodied in the standard code DLSODE[27] was used. In this method, the user requests a solution with a specified precision at the end of an external step. The software then selects internal step sizes so as to achieve this goal. For all but one species the absolute error tolerance was set at 10^{-12}. Because some species have very small, but rapidly evolving mass fractions, a simple dynamic tolerance was imposed on a limited basis: for the minor species C_2H_6, a tolerance of 10^{-25} was set in early stages of the calculation, $x \leq 2 \times 10^{-5}$ cm; for $x > 2 \times 10^{-5}$ cm, the tolerance was reset to 10^{-12}. With DLSODE, it was straightforward to adjust the external spatial discretization step so as to generate detailed results in the induction zone, and coarser results near equilibrium. However, even near equilibrium, it was seen that the number of internal steps taken to achieve the error tolerance was consistent with the discretization at the spatial scale dictated by the finest physical scale.

IV. Results

Results are focused on stoichiometric methane oxidation. A kinetic model with $N = 21$ species (19 of which are reactive), $L = 5$ atomic elements, and $J = 52$ reversible reactions, nearly identical to that employed by Yungster and Rabinowitz[10] in their methane-air calculations, is used. The twenty-one species modeled are H_2, H, O, O_2, OH, H_2O, HO_2, H_2O_2, CH_3, CH_4, CO, CO_2, CHO, CH_2O, CH_3O, C_2H_3, C_2H_4, C_2H_5, C_2H_6, N_2 and Ar. Nitrogen and argon are regarded as inert diluents. The five atomic elements are H, O, C, N, and Ar. Reactions and high pressure kinetic rate parameters are listed in Table 1. Dimensionless third body enhancement factors, η_i, are listed in Table 2. Some minor changes were made to the kinetic model of Ref. 10. First, Ref. 10 employed three reactions (33, 48, and 49) with pressure-dependent rates; however, the interpolation coefficients which dictate the rate fall-off were not given in a form which was transparently able to be utilized with the CHEMKIN software package. Consequently, kinetic data for these three reactions were taken from a standard alternate source.[12] Low pressure kinetic rate parameters and Troe centering parameters for these three reactions are listed in Table 3. Second, Ref. 10 did not consider Ar, which is admitted here in order to compare predictions against some experimental data. Coefficients $a_{1i}, \ldots, a_{7i}$ for polynomial curve fits from GRI 3.0[12] for c_{pi}, h_i^o, and s_i^o are listed in Tables 4 and 5 to three significant figures; actual calculations utilized the nine significant figures given in Ref. 12. Table 4 fits the data well for 1000 $K < T < 3500$ K and is used for the bulk of the calculations in the reaction zone past the shock. Table 5 is valid for lower temperatures, 200 $K < T < 1000$ K, found before the lead shock; only species modeled as present before the lead shock are included in Table 5.

A. Mathematical Verification

A necessary condition for a mathematically verified model is that it yield the same predictions as have been obtained by previous researchers exercising the same model. One common test is to compute t_{ign} in a spatially homogeneous adiabatic, isobaric time-dependent system. Here, t_{ign} is mathematically defined as the time at which d^2T/dt^2 crosses zero; i.e., an inflection point of $T(t)$. Ref. 10 provides such calculations based on conditions cited in Ref. 11, which are in fact difficult to discern; thus, these calculations could not be repeated. However, Ref. 13 provides calculations of t_{ign} using the kinetic model of Ref. 10 as well as sufficient details to reproduce their results. Ref. 13 is mainly concerned with high pressure combustion of fuel-rich mixtures, and they find that the kinetic model of Ref. 10 gives reliable predictions as long as

the initial temperature is above a threshold value. Here, comparisons are given in Table 6 for the case documented in Fig. 1 of Ref. 13 for a mixture of $3CH_4 + 2O_2 + 10N_2$ at $p_o = 150\ atm$, $1333 \leq T_o \leq 1500\ K$. Agreement is good.

A second qualitative method of mathematical verification is to examine results for different error tolerances and determine if new flow structures arise. Though not reported here, this was done, and no new structures were predicted as tolerances were reduced, although for coarse tolerances, numerical roundoff errors become apparent for minor species mass fractions, and for extremely fine tolerances, local iterative convergence becomes more difficult. As demonstrated in Ref. 8, a more robust mathematical verification is given by detailed convergence studies in which computational step sizes are systematically varied and the rate at which error norms approach zero are compared to the inherent order of convergence of the numerical method. This was not performed here, but as the same method and code were used as in robustly verified Ref. 8, there is no real reason for concern.

B. Validation with Experiment

When one is confident that the computational predictions of the model are behaving in a fashion consistent with its underlying mathematics, it is appropriate to consider how well its predictions match experiment. There are two validation tests in common usage: 1) comparison with measured ignition delay times, and 2) correlation of predicted induction zone lengths, ℓ_{ind}, with measured detonation cell widths, ℓ_{cell}. Here, ℓ_{ind} is defined as the distance at which d^2T/dx^2 crosses zero, i.e. the inflection point in $T(x)$. Of these, 1) is the more reliable, as 2) is the consequence of a fully three-dimensional unsteady phenomena, which is beyond the capability of a one-dimensional steady state model. However, as exemplified in Ref. 15, there is a long history of attempting to correlate three-dimensional cell sizes with the predictions of one-dimensional theory. Ratios of ℓ_{cell}/ℓ_{ind} between 10 and 40 are common in hydrocarbon mixtures. It is recognized that both these validations are incomplete in many ways; for example, neither provide fine scale data for minor species.

1. *Spatially Homogeneous Ignition Delay Time*

Spadaccini and Colket[14] provide a large data set of ignition delay times for methane oxidation. Nine of their cases were selected for comparison, each of which considered the stoichiometric mixture $0.035CH_4 + 0.070O_2 + 0.895Ar$ at various p_o and T_o. Comparisons are shown in Table 7, and the degree of agreement is quantified in Eqs. (43-44):

$$t_{ign}^{exp} \sim \left(2.21 \times 10^{-4}\ s\right) - \left(2.73 \times 10^{-3}\ s\right)\left(\frac{T_o - 1718.56\ K}{1718.56\ K}\right) + \left(2.20 \times 10^{-5}\ s\right)\left(\frac{p_o - 6.24\ atm}{6.24\ atm}\right), \quad (43)$$

$$t_{ign}^{comp} \sim \left(2.48 \times 10^{-4}\ s\right) - \left(3.54 \times 10^{-3}\ s\right)\left(\frac{T_o - 1718.56\ K}{1718.56\ K}\right) + \left(1.04 \times 10^{-4}\ s\right)\left(\frac{p_o - 6.24\ atm}{6.24\ atm}\right). \quad (44)$$

Each of these are linear least squares curve fits of $t_{ign}(T_o, p_o)$ to the experimental data and computational predictions, respectively, centered about the mean values of T_o and p_o. Clearly, the model does best in capturing the correct mean value and temperature sensitivity. The relative pressure sensitivity has the correct sign, but differs by an order of magnitude from the measured value. There is also a much stronger sensitivity to relative changes in temperature instead of pressure.

2. *Comparison with Detonation Cell Size*

For a stoichiometric methane-air mixture with an initial state of $CH_4 + 2O_2 + 7.52N_2$ and $p_o = 1\ atm$, Tieszen, et al.[15] measure ℓ_{cell} and use their own kinetic model to predict ℓ_{ind} at two different initial temperatures: $T_o = 298\ K$ and $373\ K$. The present model was exercised under the same conditions, comparisons are given in Table 8. Once again, agreement is good.

The detonation was modeled at near-CJ conditions; the precise CJ state is achieved when the states of chemical equilibrium and $\mathsf{M} = 1$ are achieved simultaneously. As described by Fickett and Davis,[26] rigorous steady detonation theory only has shown the CJ state to be the speed of propagation of an unsupported wave for irreversible exothermic reactions. Most other detonation models, including those with reversible reaction rates such as considered here, admit solutions which are perturbations of the CJ state. For reactions dominated by strong exothermicity in the forward rate, the deviation from CJ is small. Consequently, the results here, labeled "CJ," actually represent a solution with as small an overdrive as possible to prevent

a sonic point from being reached at a point where the reaction was not in equilibrium. This state was determined by iteration.

C. Stoichiometric Near-CJ Methane-Air Detonation at Standard Conditions

With confidence that the kinetic model was verified and validated to a presently accepted, albeit imperfect, standard, a detailed examination was undertaken of a minimally overdriven, near-CJ, detonation of a stoichiometric mixture of $CH_4 + 2O_2 + 7.52N_2$, which in its unshocked state was at $p_o = 1\ atm$ and $T_o = 298\ K$. Values of various thermochemical and dynamic properties at the initial state, shock state, and equilibrium state are given in Table 9.

Figure 1 gives a plot of the spatial distribution of species mass fractions throughout the reaction zone. The use of log-log scaling in Fig. 1 reveals a variety of scales over which the mass fractions evolve. The shock front is located at $x = 0\ cm$. Just past the shock, collisions of the major species CH_4, O_2, and N_2 commence with more vigor, and minor species are generated. For small distances from the shock front $0 < x < 10^{-4}\ cm$, the mass fractions of minor species grow at rates which are well modeled by power laws, while major species mass fractions are essentially unchanged. At $x \sim 10^{-4}\ cm$, one notices the slopes of the curves begin to change; this indicates that, at this scale, there is beginning to be significant chemical interactions of the minor species. For $10^{-4} < x < 10^{0}\ cm$, major species collisions continue, minor species mass fractions continue to rapidly grow, and the minor species continue to interact. Just past $x = 10^{0}\ cm$, a particularly vigorous stage of the reaction ensues in which all species mass fractions, except the inert N_2, undergo significant change. This region is considered to be near the end of the induction zone, whose thickness is given by $\ell_{ind} = 1.58 \times 10^{0}\ cm$. It is also the beginning of the thermal explosion zone, which extends from roughly $1.58 \times 10^{0} < x < 1.60 \times 10^{0}\ cm$. This is followed by a relatively long recombination zone, $1.60 \times 10^{0} < x < 10^{1}\ cm$, in which radicals recombine exothermically into the predominant product species, H_2O and CO_2. For $x > 10^{1}\ cm$, it is clear from Fig. 1 that the system has come to an equilibrium, as all spatial gradients are near zero. This is confirmed by calculating the equilibrium state with an iterative Newton solver for $f_i(Y_i, \ldots, Y_{N-L}) = 0$.

The multi-scale nature of the problem is most clearly displayed in Fig. 2. Here, the length scales $\ell_i(x)$ predicted by the local eigenvalue analysis described earlier are shown as functions of the distance from the shock. Each curve corresponds to the reciprocal of the absolute value of the real part of an eigenvalue. Most importantly, the finest length scale is seen to vary from near $10^{-4}\ cm$ in the induction zone to as low as $\ell_f = 1.04 \times 10^{-5}\ cm$ in the recombination zone. The largest length scales range from around $10^{8}\ cm$ in the induction zone to around $10^{0}\ cm$ at equilibrium state. The smallest length scale is consistent with the scale on which mass fractions are seen to vary in Fig. 1. Moreover, the smallest scale is roughly equal to the internal step size utilized by the adaptive DLSODE integration subroutine, in which the size of the integration step is automatically chosen to maintain stability as well as achieve the specified accuracy. The largest length scale is not as critical, but its value at equilibrium provides a useful estimate of the overall length of the reaction zone.

Additional features of Fig. 2 are noteworthy. For the bulk of the domain, there are $N - L = 16$ real and distinct eigenvalues. For $x > 2 \times 10^{0}\ cm$, the real parts of all sixteen eigenvalues are negative, indicating a relaxation to equilibrium. The spikes in some of the curves near $x = 1.5 \times 10^{0}\ cm$ indicate some of the eigenvalues have real parts passing through zero; hence, their reciprocals approach infinity. In a few isolated regions near the end of the induction zone and in the thermal explosion zone, some of the eigenvalues are complex conjugates. This is indicative of a local oscillatory behavior and is seen in Fig. 2 when some of the curves merge in a thin zone.

A plot of temperature in the reaction zone is given in Fig. 3. The induction zone is seen to be a region of essentially constant temperature. This seeming serenity cloaks a cauldron of activity as species mass fractions evolve rapidly within this zone. In contrast, the evolution of temperature in the recombination zone is mild in comparison.

V. Equivalence to the Molecular Collision Length Scale

The most striking result of the previous section is the dramatically small length scale, $\sim 10^{-5}\ cm$, that must be considered in order to claim a fully resolved, direct numerical simulation (DNS). Ref. 8 showed essentially the same result for $H_2/O_2/N_2$ mixtures and went on to show that no existing calculation of

unsteady detonation flow fields with detailed kinetics has employed sufficiently fine grid scales to resolve all flow structures inherent to the chosen mathematical model. A common, but flawed, defense of calculations with overly coarse grids is that detailed kinetics models are not appropriate as scales approach mean free path distances, and only should be used on scales which encompass at least dozens, if not hundreds, of mean free paths. This section will appeal to continuum mechanics and its underlying collision theory to argue that such a defense is, in fact, groundless.

Rational continuum theories, as exemplified in Eqs. (1-18), rely upon constitutive models whose constants can be deduced either from 1) experiment, or 2) averaging methods applied to a more fundamental underlying model valid at a smaller, sub-continuum, scale. It is well known, cf. Vincenti and Kruger,[28] that diffusive transport properties such as viscosity and thermal conductivity, as well as reaction parameters such as A_j, Θ_j, and β_j, can be directly related to molecular properties. For example, for simple dissociation recombination reactions, Ref. 28 estimate in their Eq. (VII.6.7b) the continuum constitutive theory parameters A_j and β_j. In a simplified limit, this reduces to

$$A_j \sim 2\mathsf{N}\mathsf{d}^2\sqrt{\frac{2\pi\mathsf{k}}{\mathsf{m}}}, \qquad \beta_j = \frac{1}{2}, \tag{45}$$

where new parameters, described in detail on p. 25 of Ref. 28, are $\mathsf{N} = 6.02 \times 10^{23}\ 1/mole$, Avogadro's number; $\mathsf{k} = \Re/\mathsf{N} = 1.38 \times 10^{-16}\ erg/K$, the Boltzmann constant; m, the mass of a molecule, and d, the molecular collision cross-section diameter. Adopting Ref. 28's estimate of $\mathsf{d} = 3.7 \times 10^{-7}\ cm$ for air, calculating $\mathcal{M} = 27.1\ g/mole$, the mixture molar mass at the CJ state, estimating $\mathsf{m} = \mathcal{M}/\mathsf{N} = (27.1\ g/mole)/(6.02 \times 10^{23}\ 1/mole) = 4.50 \times 10^{-23}\ g$, one finds that Eq. (45) yields an estimate of $A_j \sim 7.24 \times 10^{12}\ cm^3/mole/s/K^{1/2}$. As discussed in Ref. 22, p. 411, such estimates are not largely different from actual values used in calculation for simple atomic and diatomic molecules; however, they can yield errors of many orders of magnitude for uni-molecular reactions and reactions involving complex molecules. And while actual reaction rate estimates typically have collision theory as their foundation, there is a host of refinements, e.g. transition state theory, developed over the decades by kineticists; Ref. 22 provides a modern summary. Whatever refinement might exist, once constructed, continuum theories can be queried to yield results at any length scale; however, one must realize that the results are physically meaningful *at or above* a cutoff length scale. Below the cutoff length scale, continuum theories continue to yield predictions. However, these predictions exhibit no additional structures and simply interpolate between the structures found above the cutoff length scale, yielding results valid only in an average sense.

For continuum theories whose constitutive model parameters are averaged manifestations of molecular collision theories, the cutoff length scale is ℓ_{mfp}, the mean free path distance between collisions. Ref. 28 in their Eq. (I.4.3b) gives a simple estimate for ℓ_{mfp}:

$$\ell_{mfp} \sim \frac{\mathsf{m}}{\sqrt{2}\pi\mathsf{d}^2\rho}, \tag{46}$$

Taking the CJ density of $\rho = 2.04 \times 10^{-3}\ g/cm^3$, one estimates $\ell_{mfp} \sim 3.6 \times 10^{-6}\ cm$. This estimate is well correlated with the actual $\ell_f = 1.04 \times 10^{-5}\ cm$ predicted by the eigenvalue analysis and reported in Table 8, and so provides additional evidence in support of the eigenvalue analysis. A plot of ℓ_{mfp}, ℓ_f, and ℓ_{ind} for CJ detonation in a mixture of $CH_4 + 2O_2 + 7.52N_2$ at $T_o = 298\ K$ and various p_o is given in Fig. 4. The estimates from Eq. (46) agree well the predictions of ℓ_f from the eigenvalue analysis. And both are roughly three orders of magnitude finer than ℓ_{ind} under the same conditions.

It is also easy to show that ℓ_{mfp} is the foundational cutoff length scale for *all* continuum theories of gas dynamics, and that it applies equally as well to mass, momentum, and energy diffusion mechanisms in addition to reaction. And, though often unrecognized in much of the aerospace propulsion community, it has long been known that continuum theories can excel in predicting phenomena at scales *at or above* ℓ_{mfp}. A well documented example which considers finite width viscous structures for shocks of moderate strength is summarized in Ref. 28, pp. 412-24. Here, it is clearly seen that predictions of temperature given by a continuum Navier-Stokes theory agree well with both 1) experiment, and 2) predictions of a more robust theory based on a non-continuum Burnett theory. As stated by Ref. 28, "...comparisons with experiment show that the Navier-Stokes solution is accurate for larger values of [Mach number] then [*sic*] might be expected from purely theoretical considerations....It is sometimes said that the test of a good theory is whether its usefulness exceeds its expected range of validity; the Navier-Stokes equations amply satisfy this criterion." As M increases, the shock wave becomes thinner, gradients become steeper, and higher order

non-continuum effects, neglected by the Navier-Stokes theory, become more important. However, even for $\mathsf{M} = 5$ flow, Fig. 4, p. 423 of Ref. 28 shows a Navier-Stokes solution has a high degree of fidelity with the predictions of a non-continuum theory.

Note further that for compressible flow, the so-called Kolmogorov scale of turbulence is one and the same with the scale of shock thicknesses, which itself is on the order of ℓ_{mfp}, as can be shown by simple scaling arguments.[29] Thus, for a compressible flow with elementary reactions, *all* finest scales are related to the mean free path. The common flamelet approach in which some fine scale flame structures are not resolved in some low Mach number simulations of combustion loses its physical rationale for a DNS[30] of detonation. In summary, then, one can say that a true DNS of compressible reactive flow with detailed kinetics which has full fidelity with the underlying molecular collision theory needs to include all collision-based mechanisms, both for reaction and diffusion of mass, momentum, and energy. The common justification for reactive Euler equations that diffusion can be neglected relative to reaction is not true when one considers a fully resolved calculation with detailed kinetics. That said, reactive Euler equations retain value for qualitative studies used to predict trends.

VI. Necessary Grid Resolution for Previously Published Studies

As detailed kinetics models are often coupled with fluid flow models in aero-propulsion computational studies, it is instructive to compare the grid resolution employed in such studies[10,17–20] with that which is necessary for complete resolution of continuum reaction length scales intrinsic to the chosen model of the studies. It can be difficult to precisely determine the grid sizes and induction lengths from published reports; sometimes even rough estimates are impossible. In the interest of scientific reproducibility, it is imperative that such parameters and results be reported. Most important for grid resolution issues is to clearly state sufficient information so that the physical size of the smallest grid dimension can be determined; the common practice of reporting only the number of grid points without the corresponding dimensions of the domain is insufficient. Whatever the case, best estimates have been made, and results are summarized in Table 10. Obviously, the previously published results have not resolved the scales by several orders of magnitude.

The fact that detailed kinetics models demand fine spatial resolution has not been lost upon some researchers, who have explicitly chosen simpler kinetic models tailored specifically so as to avoid the necessity of modeling at this scale. Such an approach is well exemplified by the study of Bielert and Sichel,[31] who employ a front-tracking model to describe one-dimensional DDT in a methane-air mixture. Their conclusion, albeit directed towards turbulent combustion with detailed kinetics, remains, with two caveats, true today: that computation "...in complex geometries with detailed kinetics is still beyond the capacities of modern computers." The caveats are 1) that the largest geometries have common aerospace engineering maximum length scales, e.g. 10^3 *cm*, and 2) no adaptive mesh refinement, such as employed in recent calculations of $H_2/O_2/Ar$ detonations[32] and useful when a small number of regions with steep gradients is present, is employed.

VII. Conclusions

The present results conclusively confirm that continuum models of methane-based compressible reactive flow contain the same small (10^{-5} *cm*) mean free path length scales previously recognized[8] in combustion of hydrogen-based mixtures. The direct linkage, shown originally here, of the eigenvalue-predicted length scales with the predictions of molecular collision theory suggests this conclusion will hold for any collision-based continuum theory; there should be no need for a series of studies for every conceivable gas mixture.

These small scales, when attached to problems with much larger engineering scales, e.g. 10^3 *cm*, pose a true multi-scale grand challenge; the ratio of scales is as much as 10^8. In fact, it is demonstrated in Ref. 2 that even with the best of modern supercomputers with up to 3.2×10^{13} *byte RAM*, the largest breadth of scales for one-, two-, and three-dimensional aero-propulsion problems that can be loaded into random access memory is roughly 10^{12}, 10^6, and 10^4, respectively. On such a machine, assuming the smallest length scale is 10^{-5} *cm*, the largest one-, two-, and three-dimensional devices that could be simulated have linear dimensions of 10^7 *cm*, 10^1 *cm*, and 10^{-1} *cm*, respectively. On a more ordinary desktop computer with 10^9 *byte RAM*, the equivalent peak dimensions are 10^3 *cm*, 10^{-1} *cm*, and 10^{-3} *cm*, respectively. To summarize, for aero-propulsion devices with common engineering geometric scales, it is presently possible to consider flow with resolved detailed kinetics in one spatial dimension on desktop machines and two

spatial dimensions on modern supercomputers. And this only speaks to the ability to load a problem into memory; a time-dependent calculation still may be prohibitively expensive if the simulation time is too long. Adaptive gridding can moderate these conclusions for flows in which steep gradients are confined to a few small regions. However, many computational challenges remain for adaptation in a dynamic environment; moreover, adaptation is of little use when regions of steep gradient are distributed throughout the domain, as can be common in turbulent combusting environments.

Now, it is clear that in order to address problems of technological interest, detailed kinetic mechanisms are being used and will be used even more so in the foreseeable future. There are at present two challenges that a researcher encounters in achieving and reporting reproducible results. The first challenge is the requirement of appropriate resolution of all scales embodied in the model. If insufficient resolution is used due to lack of computational resources, this should be acknowledged and the conclusions appropriately tempered. The second challenge is in reporting sufficient details so that results can be reproduced. While it is recognized that the standard for scientific reproducibility requires that the problem's details be provided, we realize that it is impractical to routinely publish extensive tables of detailed mechanisms and associated thermodynamic data. Thus, we strongly advocate the creation and maintenance of a standard database to which all researchers can refer in published works.

In conclusion, it is recommended that the aero-propulsion modeling community aspire to present numerical computations which are first mathematically verified and second experimentally validated.[6,7] Such an exercise is necessary to fully realize the goal of predictive, science-based design and engineering. Moreover, it is clear that many predictions with detailed kinetics do not agree with observation; perhaps the reason is because of lack of proper resolution. It thus should be axiomatic that modern computational predictions should accurately reflect the true solution of the underlying mathematical model, however simple or complex that model may be.

References

[1] Oran, E. S., "Matchsticks, Scramjets, and Black Holes: Numerical Simulation Faces Reality," *AIAA Journal*, Vol. 40, No. 8, 2002, pp. 1481-1494.

[2] Powers, J. M., "Review of Multiscale Modeling of Detonation," *Journal of Propulsion and Power*, to appear, 2006.

[3] Leblanc, J. E., Nusca, M., Wang, X., Seiler, F., Sugihara, M., and Fujiwara, T., "Numerical Simulation of the RAMAC Benchmark Test," *Journal de Physique IV*, Vol. 10, No. 11, 2000, pp. 119-130.

[4] Tangirala, V. E., Dean, A. J., Chapin, D. M., Pinard, P. F., and Varatharajan, B., "Pulsed Detonation Engine Processes: Experiments and Simulations," *Combustion Science and Technology*, Vol. 176, No. 10, 2004, pp. 1779-1808.

[5] Kadanoff, L. P., "Excellence in Computer Simulation," *Computing in Science and Engineering*, Vol. 6, No. 2, 2004, pp. 57-67.

[6] Roache, P. J., "Quantification of Uncertainty in Computational Fluid Dynamics," *Annual Review of Fluid Mechanics*, Vol. 29, 1997, pp. 123-160.

[7] Oberkampf, W. L., and Trucano, T. G., "Verification and Validation in Computational Fluid Dynamics," *Progress in Aerospace Sciences*, Vol. 38, No. 3, 2002, pp. 209-272.

[8] Powers, J. M., and Paolucci, S., "Accurate Spatial Resolution Estimates for Reactive Supersonic Flow with Detailed Chemistry," *AIAA Journal*, Vol. 43, No. 5, 2005, pp. 1088-1099.

[9] "Editorial Policy Statement of Numerical Accuracy and Experimental Uncertainty," *AIAA Journal*, Vol. 43, No. 1, 2005, p. 14.

[10] Yungster, S., and Rabinowitz, M. J., "Computation of Shock-Induced Combustion Using a Detailed Methane-Air Mechanism," *Journal of Propulsion and Power*, Vol. 10, No. 5, 1994, pp. 609-617.

[11] Frenklach, M., Wang, H., and Rabinowitz, M. J., "Optimization and Analysis of Large Chemical Kinetic Mechanisms Using the Solution Mapping Method–Combustion of Methane," *Progress in Energy and Combustion Science*, Vol. 18, No. 1, 1992, pp. 47-73.

[12] Smith, G. P., Golden, D. M., Frenklach, M., Moriarty, N. W., Eiteneer, B., Goldenberg, M., Bowman, C. T., Hanson, R. K., Song, S., Gardiner, W. C., Lissianski, V. V., and Qin, Z., "GRI-Mech 3.0," URL: http://www.me.berkeley.edu/gri_mech [cited 1 December 2005].

[13] Petersen, E. L., and Hanson, R. K., "Reduced Kinetics Mechanisms for Ram Accelerator Combustion," *Journal of Propulsion and Power*, Vol. 15, No. 4, 1999, pp. 591-600.

[14] Spadaccini, L. J., and Colket, M. B., "Ignition Delay Characteristics of Methane Fuels," *Progress in Energy and Combustion Science*, Vol. 20, No. 5, 1994, pp. 431-460.

[15] Tieszen, S. R., Stamps, D. W., Westbrook, C. K., and Pitz, W. J., "Gaseous Hydrocarbon-Air Detonations," *Combustion and Flame*, Vol. 84, Nos. 3-4, 1991, pp. 376-390.

[16] Law, C. K., Sung, C. J., Wang, H., and Lu, T. F., "Development of Comprehensive Detailed and Reduced Reaction Mechanisms for Combustion Modeling," *AIAA Journal*, Vol. 41, No. 9, 2003, pp. 1629-1646.

[17] Sheffer, S. G., Martinelli, L., and Jameson, A., "Simulation of Supersonic Reacting Hydrocarbon Flows with Detailed Chemistry," *Combustion Science and Technology*, Vol. 136, Nos. 1-6, 1998, pp. 55-80.

[18] Toshimitsu, K., Matsuo, A., Kamel, M. R., Morris, C. I., and Hanson, R. K., "Numerical Simulations and Planar Laser-Induced Fluorescence Imaging Results of Hypersonic Reactive Flows," *Journal of Propulsion and Power*, Vol. 16, No. 1, 2000, pp. 16-21.

[19] Kim, S.-L., Choi, J.-Y., Jeung, I.-S., and Park, Y.-H., "Application of Approximate Chemical Jacobians for Constant Volume Reaction and Shock-Induced Combustion," *Applied Numerical Mathematics*, Vol. 39, No. 1, 2001, pp. 87-104.

[20] Parra-Santos, M. T., Castro-Ruiz, F., and Méndez-Bueno, C., "Numerical Simulation of the Deflagration to Detonation Transition," *Combustion, Explosion, and Shock Waves*, Vol. 41, No. 2, 2005, pp. 215-222 (in translation).

[21] Kuo, K. K., *Principles of Combustion*, Second Edition, John Wiley, Hoboken, New Jersey, 2005, pp. 166-168.

[22] Kee, R. J., Coltrin, M. E., and Glarborg, P., *Chemically Reacting Flow: Theory and Practice*, John Wiley, Hoboken, New Jersey, 2003, pp. 387-393.

[23] Gilbert, R. G., Luther, K., and Troe, J., "Theory of Thermal Unimolecular Reactions in the Fall-Off Range.2. Weak Collision Rate Constants," *Berichte der Bunsen-Gesellschaft-Physical Chemistry Chemical Physics*, Vol. 87, No. 2, 1983, pp. 169-177.

[24] Kee, R. J., Rupley, F. M., and Miller, J. A., "Chemkin-II: A Fortran Chemical Kinetics Package for the Analysis of Gas Phase Chemical Kinetics," Sandia National Labs., Rept. SAND89-8009B, Livermore, California, Nov. 1991.

[25] Kee, R. J., Rupley, F. M., and Miller, J. A., "The Chemkin Thermodynamic Data Base," Sandia National Laboratories Report, Rept. SAND87-8215B, Livermore, California, March 1990.

[26] Fickett, W., and Davis, W. C., *Detonation*, Univ. of California, Berkeley, California, 1979, Chap. 5.

[27] Hindmarsh, A. C., "ODEPACK, a Systematized Collection of ODE Solvers," *Scientific Computing*, edited by R. S. Stepleman, M. Carver, R. Peskin, W. F. Ames, and R. Vichnevetsky, North Holland, Amsterdam, 1983, pp. 55-64.

[28] Vincenti, W. G., and Kruger, C. H., *Introduction to Physical Gas Dynamics*, John Wiley, New York, 1965.

[29] Moin, P., and Mahesh, K., "Direct Numerical Simulation: A Tool in Turbulence Research," *Annual Review of Fluid Mechanics*, Vol. 30, 1998, pp. 539-578.

[30] Vervisch, L, and Poinsot, T., "Direct Numerical Simulation of Non-Premixed Turbulent Flames," *Annual Review of Fluid Mechanics*, Vol. 30, 1998, pp. 655-691.

[31] Bielert, U., and Sichel, M., "Numerical Simulation of Premixed Combustion Processes in Closed Tubes," *Combustion and Flame*, Vol. 114, Nos. 3-4, 1998, pp. 397-419.

[32] Singh, S., Rastigejev, Y., Paolucci, S., and Powers, J. M., "Viscous Detonation in $H_2 - O_2 - Ar$ Using Intrinsic Low-Dimensional Manifolds and Wavelet Adaptive Multilevel Representation," *Combustion Theory and Modelling*, Vol. 5, No. 2, 2001, pp. 163-184.

j	Reaction	A_j	β_j	Θ_j
1	$H + O_2 \rightleftharpoons OH + O$	1.59×10^{17}	-0.927	8491.28
2	$O + H_2 \rightleftharpoons OH + H$	3.87×10^{4}	2.700	3151.16
3	$OH + H_2 \rightleftharpoons H_2O + H$	2.16×10^{8}	1.510	1725.92
4	$OH + OH \rightleftharpoons O + H_2O$	2.10×10^{8}	1.400	-199.65
5	$H + H + M \rightleftharpoons H_2 + M$	6.40×10^{17}	-1.000	0.00
6	$H + OH + M \rightleftharpoons H_2O + M$	8.40×10^{21}	-2.000	0.00
7	$H + O_2 + M \rightleftharpoons HO_2 + M$	7.00×10^{17}	-0.800	0.00
8	$HO_2 + H \rightleftharpoons OH + OH$	1.50×10^{14}	0.000	505.15
9	$HO_2 + H \rightleftharpoons H_2 + O_2$	2.50×10^{13}	0.000	348.79
10	$HO_2 + O \rightleftharpoons O_2 + OH$	2.00×10^{13}	0.000	0.00
11	$HO_2 + OH \rightleftharpoons H_2O + O_2$	6.02×10^{13}	0.000	0.00
12	$H_2O_2 + M \rightleftharpoons OH + OH + M$	1.00×10^{17}	0.000	22851.89
13	$CO + OH \rightleftharpoons CO_2 + H$	1.22×10^{7}	1.350	-317.52
14	$CO + O + M \rightleftharpoons CO_2 + M$	3.01×10^{14}	0.000	1515.44
15	$CHO + H \rightleftharpoons CO + H_2$	7.23×10^{13}	0.000	0.00
16	$CHO + O \rightleftharpoons CO + OH$	3.00×10^{13}	0.000	0.00
17	$CHO + OH \rightleftharpoons CO + H_2O$	1.00×10^{14}	0.000	0.00
18	$CHO + O_2 \rightleftharpoons CO + HO_2$	4.20×10^{12}	0.000	0.00
19	$CHO + M \rightleftharpoons CO + H + M$	1.86×10^{17}	-1.000	8551.42
20	$CH_2O + H \rightleftharpoons CHO + H_2$	1.26×10^{8}	1.620	1094.49
21	$CH_2O + O \rightleftharpoons CHO + OH$	3.50×10^{13}	0.000	1768.01
22	$CH_2O + OH \rightleftharpoons CHO + H_2O$	7.23×10^{5}	2.460	-488.31
23	$CH_2O + O_2 \rightleftharpoons CHO + HO_2$	1.00×10^{14}	0.000	20085.61
24	$CH_2O + CH_3 \rightleftharpoons CHO + CH_4$	8.91×10^{-13}	7.400	-481.09
25	$CH_2O + M \rightleftharpoons CHO + H + M$	5.00×10^{16}	0.000	38487.40
26	$CH_3 + O \rightleftharpoons CH_2O + H$	8.43×10^{13}	0.000	0.00
27	$CH_3 + OH \rightleftharpoons CH_2O + H_2$	8.00×10^{12}	0.000	0.00
28	$CH_3 + O_2 \rightleftharpoons CH_3O + O$	4.30×10^{13}	0.000	15503.20
29	$CH_3 + O_2 \rightleftharpoons CH_2O + OH$	5.20×10^{13}	0.000	17559.87
30	$CH_3 + HO_2 \rightleftharpoons CH_3O + OH$	2.28×10^{13}	0.000	0.00
31	$CH_3 + CHO \rightleftharpoons CH_4 + CO$	3.20×10^{11}	0.500	0.00
32	$CH_3 + CH_3 \rightleftharpoons C_2H_5 + H$	4.90×10^{12}	0.000	5905.41
33[a]	$H + CH_3(+M) \rightleftharpoons CH_4(+M)$	1.39×10^{16}	-0.534	269.75
34	$CH_4 + H \rightleftharpoons CH_3 + H_2$	7.80×10^{6}	2.110	3896.85
35	$CH_4 + O \rightleftharpoons CH_3 + OH$	1.90×10^{9}	1.440	4365.91
36	$CH_4 + O_2 \rightleftharpoons CH_3 + HO_2$	5.60×10^{12}	0.000	28179.99
37	$CH_4 + OH \rightleftharpoons CH_3 + H_2O$	1.50×10^{6}	2.130	1226.79
38	$CH_4 + HO_2 \rightleftharpoons CH_3 + H_2O_2$	4.60×10^{12}	0.000	9056.57
39	$CH_3O + H \rightleftharpoons CH_2O + H_2$	2.00×10^{13}	0.000	0.00
40	$CH_3O + OH \rightleftharpoons CH_2O + H_2O$	5.00×10^{12}	0.000	0.00
41	$CH_3O + O_2 \rightleftharpoons CH_2O + HO_2$	4.28×10^{-13}	7.600	-1775.23
42	$CH_3O + M \rightleftharpoons CH_2O + H + M$	1.00×10^{14}	0.000	12628.68
43	$C_2H_3 + O_2 \rightleftharpoons CH_2O + CHO$	3.98×10^{12}	0.000	-120.27
44	$C_2H_4 + H \rightleftharpoons C_2H_3 + H_2$	3.16×10^{11}	0.700	4029.15
45	$C_2H_4 + OH \rightleftharpoons C_2H_3 + H_2O$	3.00×10^{13}	0.000	1503.41
46	$C_2H_5 + H \rightleftharpoons C_2H_4 + H_2$	3.00×10^{13}	0.000	0.00
47	$C_2H_5 + O_2 \rightleftharpoons C_2H_4 + HO_2$	2.00×10^{12}	0.000	2513.71
48[a]	$H + C_2H_4(+M) \rightleftharpoons C_2H_5(+M)$	5.40×10^{11}	0.454	915.95
49[a]	$CH_3 + CH_3(+M) \rightleftharpoons C_2H_6(+M)$	6.77×10^{16}	-1.180	329.14
50	$C_2H_6 + H \rightleftharpoons C_2H_5 + H_2$	5.40×10^{2}	3.500	2621.95
51	$C_2H_6 + OH \rightleftharpoons C_2H_5 + H_2O$	2.20×10^{7}	1.900	565.28
52	$C_2H_6 + CH_3 \rightleftharpoons C_2H_5 + CH_4$	5.50×10^{-1}	4.000	4173.48

Table 1. Twenty-one species (nineteen reacting), fifty-two step skeletal reversible reaction mechanism for a methane/oxygen/nitrogen/argon mixture from Yungster and Rabinowitz,[10] with three substitutions[a] from GRI 3.0.[12] Units of Θ_j are K. Units of A_j are such that the species production rate has units of $mole/cm^3/s$; β_j is dimensionless. Third body enhancement coefficients are given in Table 2. For pressure-dependent reactions[a], $A_j = A_j^{\infty}$, $\beta_j = \beta_j^{\infty}$, and $\Theta_j = \Theta_j^{\infty}$; low pressure coefficients are given in Table 3.

j	η_{H_2}	η_{O_2}	η_{N_2}	η_{H_2O}	η_{CO}	η_{CO_2}
6	1.900×10^0	2.600×10^0	2.600×10^0	9.500×10^0	2.600×10^0	2.600×10^0
12	2.900×10^0	1.200×10^0	1.200×10^0	1.850×10^1	2.100×10^0	4.300×10^0
14	1.000×10^0	1.200×10^0	2.000×10^0	1.000×10^0	3.000×10^0	7.000×10^0
19	1.870×10^0	1.000×10^0	1.000×10^0	8.120×10^0	1.000×10^0	1.000×10^0
25	2.900×10^0	1.200×10^0	1.200×10^0	1.850×10^1	2.100×10^0	4.300×10^0
42	2.900×10^0	1.200×10^0	1.200×10^0	1.850×10^1	2.100×10^0	4.300×10^0

Table 2. Dimensionless third body enhancement factors, η_i, for selected reactions from a twenty-one species, fifty-two step reversible reaction mechanism for a methane/oxygen/nitrogen/argon mixture extracted from Yungster and Rabinowitz.[10]

j	A_j^0	β_j^0	Θ_j^0	α_j	T_j^{***}	T_j^*	T_j^{**}
33	2.620×10^{33}	-4.760×10^0	1.228×10^3	7.830×10^{-1}	7.400×10^1	2.941×10^3	6.964×10^3
48	6.000×10^{41}	-7.620×10^0	3.508×10^3	9.753×10^{-1}	2.100×10^2	9.840×10^2	4.374×10^3
49	3.400×10^{41}	-7.030×10^0	1.390×10^3	6.190×10^{-1}	7.320×10^1	1.180×10^3	9.999×10^3

Table 3. Low pressure limit kinetic rate parameters and Troe centering factors for selected reactions from a twenty-one species, fifty-two step reversible reaction mechanism for a methane/oxygen/nitrogen/argon mixture from GRI 3.0.[12] Units of Θ_j^0 are K. Units of A_j^0 are such that the species production rate has units of $mole/cm^3/s$; β_j^0 is dimensionless; α_j is dimensionless. Units for T_j^{***}, T_j^*, and T_j^{**} are K.

i	Specie	a_{1i}	a_{2i} $(1/K)$	a_{3i} $(1/K^2)$	a_{4i} $(1/K^3)$	a_{5i} $(1/K^4)$	a_{6i} (K)	a_{7i}
1	H_2	0.234×10^1	0.798×10^{-2}	-0.195×10^{-4}	0.202×10^{-7}	-0.738×10^{-11}	-0.918×10^3	0.683×10^0
2	H	0.250×10^1	0.705×10^{-12}	-0.200×10^{-14}	0.230×10^{-17}	-0.928×10^{-21}	0.255×10^5	-0.447×10^0
3	O	0.317×10^1	-0.328×10^{-2}	0.664×10^{-5}	-0.613×10^{-8}	0.211×10^{-11}	0.291×10^5	0.205×10^1
4	O_2	0.378×10^1	-0.300×10^{-2}	0.985×10^{-5}	-0.968×10^{-8}	0.324×10^{-11}	-0.106×10^4	0.366×10^1
5	OH	0.399×10^1	-0.240×10^{-2}	0.462×10^{-5}	-0.388×10^{-8}	0.136×10^{-11}	0.362×10^4	-0.104×10^0
6	H_2O	0.420×10^1	-0.204×10^{-2}	0.652×10^{-5}	-0.549×10^{-8}	0.177×10^{-11}	-0.303×10^5	-0.849×10^0
7	HO_2	0.430×10^1	-0.475×10^{-2}	0.212×10^{-4}	-0.243×10^{-7}	0.929×10^{-11}	0.295×10^3	0.372×10^1
8	H_2O_2	0.428×10^1	-0.543×10^{-3}	0.167×10^{-4}	-0.216×10^{-7}	0.862×10^{-11}	-0.177×10^5	0.344×10^1
9	CH_3	0.367×10^1	0.201×10^{-2}	0.573×10^{-5}	-0.687×10^{-8}	0.254×10^{-11}	0.164×10^5	0.160×10^1
10	CH_4	0.515×10^1	-0.137×10^{-1}	0.492×10^{-4}	-0.485×10^{-7}	0.167×10^{-10}	-0.102×10^5	-0.464×10^1
11	CO	0.358×10^1	-0.610×10^{-3}	0.102×10^{-5}	0.907×10^{-9}	-0.904×10^{-12}	-0.143×10^5	0.351×10^1
12	CO_2	0.236×10^1	0.898×10^{-2}	-0.712×10^{-5}	0.246×10^{-8}	-0.144×10^{-12}	-0.484×10^5	0.990×10^1
13	CHO	0.422×10^1	-0.324×10^{-2}	0.138×10^{-4}	-0.133×10^{-7}	0.434×10^{-11}	0.384×10^4	0.339×10^1
14	CH_2O	0.479×10^1	-0.991×10^{-2}	0.373×10^{-4}	-0.380×10^{-7}	0.132×10^{-10}	-0.143×10^5	0.603×10^0
15	CH_3O	0.211×10^1	0.722×10^{-2}	0.534×10^{-5}	-0.738×10^{-8}	0.208×10^{-11}	0.979×10^3	0.132×10^2
16	C_2H_3	0.321×10^1	0.151×10^{-2}	0.259×10^{-4}	-0.358×10^{-7}	0.147×10^{-10}	0.349×10^5	0.851×10^1
17	C_2H_4	0.396×10^1	-0.757×10^{-2}	0.571×10^{-4}	-0.692×10^{-7}	0.270×10^{-10}	0.509×10^4	0.410×10^1
18	C_2H_5	0.431×10^1	-0.419×10^{-2}	0.497×10^{-4}	-0.599×10^{-7}	0.231×10^{-10}	0.128×10^5	0.471×10^1
19	C_2H_6	0.429×10^1	-0.550×10^{-2}	0.599×10^{-4}	-0.708×10^{-7}	0.269×10^{-10}	-0.115×10^5	0.267×10^1
20	N_2	0.330×10^1	0.141×10^{-2}	-0.396×10^{-5}	0.564×10^{-8}	-0.244×10^{-11}	-0.102×10^4	0.395×10^1
21	Ar	0.250×10^1	0.000×10^0	0.000×10^0	0.000×10^0	0.000×10^0	-0.745×10^3	0.437×10^1

Table 4. Polynomial curve fit coefficients from GRI 3.0[12] for thermodynamic properties for $1000\ K \leq T < 3500\ K$.

i	Specie	a_{1i}	a_{2i} $(1/K)$	a_{3i} $(1/K^2)$	a_{4i} $(1/K^3)$	a_{5i} $(1/K^4)$	a_{6i} (K)	a_{7i}
4	O_2	0.328×10^1	0.148×10^{-2}	-0.758×10^{-6}	0.209×10^{-9}	-0.217×10^{-13}	-0.109×10^4	0.545×10^1
10	CH_4	0.749×10^{-1}	0.134×10^{-1}	-0.573×10^{-5}	0.122×10^{-8}	-0.102×10^{-12}	-0.947×10^4	0.184×10^2
20	N_2	0.293×10^1	0.149×10^{-2}	-0.569×10^{-6}	0.101×10^{-9}	-0.675×10^{-14}	-0.923×10^3	0.598×10^1
21	Ar	0.250×10^1	0.000×10^0	0.000×10^0	0.000×10^0	0.000×10^0	-0.745×10^3	0.437×10^1

Table 5. Polynomial curve fit coefficients from GRI 3.0[12] for thermodynamic properties for $200\ K < T < 1000\ K$ for species which are modeled in the unshocked state.

$T_o\ (K)$	$t_{ign}\ (s)$ Ref. 13	$t_{ign}\ (s)$ present study
1500	3.0×10^{-5}	2.51×10^{-5}
1429	6.2×10^{-5}	5.16×10^{-5}
1333	1.1×10^{-4}	1.68×10^{-4}

Table 6. Computational predictions of ignition delay times for mixtures of $3CH_4 + 2O_2 + 10N_2$ at $p_o = 150\ atm$ and various initial temperatures given by the the present twenty-one species, fifty-two step reversible reaction mechanism under isobaric spatially homogeneous conditions from two separate sources: 1) estimates extracted from Petersen and Hanson,[13] and 2) the present study.

$T_o\ (K)$	$p_o\ (atm)$	$t_{ign}\ (s)$ experimental[14]	$t_{ign}\ (s)$ present study
1705	6.55	1.15×10^{-4}	1.39×10^{-4}
1672	6.28	2.36×10^{-4}	1.87×10^{-4}
1918	7.97	2.20×10^{-5}	2.76×10^{-5}
1799	7.58	7.50×10^{-5}	6.22×10^{-5}
1516	5.78	5.93×10^{-4}	7.79×10^{-4}
1525	5.90	5.93×10^{-4}	7.04×10^{-4}
1820	8.28	4.30×10^{-5}	5.03×10^{-5}
1759	4.02	1.46×10^{-4}	1.35×10^{-4}
1753	3.77	1.71×10^{-4}	1.49×10^{-4}

Table 7. Ignition delay times for mixtures of $0.035CH_4 + 0.070O_2 + 0.895Ar$ at various initial temperatures and pressures as measured in experiment[14] and predicted by the present twenty-one species, fifty-two step reversible reaction mechanism under isobaric spatially homogeneous conditions.

$T_o\ (K)$	$\ell_{cell}\ (cm)$ Ref. 15	$\ell_{ind}\ (cm)$ Ref. 15	$\ell_{ind}\ (cm)$ present study	$\ell_f\ (cm)$ present study	$D_{CJ}\ (cm/s)$
298	30.5	2.76	1.58	1.04×10^{-5}	1.81053×10^5
373	26.0	2.37	1.41	1.27×10^{-5}	1.80439×10^5

Table 8. Experimentally observed[15] detonation cell widths ℓ_{cell}, predictions of induction zone lengths ℓ_{ind}, and finest collision-based length scale ℓ_f for near-CJ detonations for mixtures of $CH_4 + 2O_2 + 7.52N_2$ initially at $p_o = 1\ atm$ and various initial temperatures.

Property	Units	Initial	Shock	CJ
p	atm	1.00000×10^{0}	3.16139×10^{1}	1.73128×10^{1}
T	K	2.98000×10^{2}	1.53240×10^{3}	2.79971×10^{3}
u	cm/s	1.81053×10^{5}	2.94498×10^{4}	1.00271×10^{5}
ρ	g/cm^3	1.13011×10^{-3}	6.94776×10^{-3}	2.04058×10^{-3}
e	erg/g	-3.46389×10^{9}	8.77863×10^{9}	1.99057×10^{8}
c_p	$erg/g/K$	1.07682×10^{7}	1.46889×10^{7}	1.54873×10^{7}
c_v	$erg/g/K$	7.75954×10^{6}	1.16802×10^{7}	1.24167×10^{7}
γ		1.38774×10^{0}	1.25759×10^{0}	1.24729×10^{0}
c	cm/s	3.52738×10^{4}	7.61456×10^{4}	1.03550×10^{5}
M		5.13279×10^{0}	3.86757×10^{-1}	9.68338×10^{-1}
Y_{H_2}		0.00000×10^{0}	0.00000×10^{0}	5.98774×10^{-4}
Y_H		0.00000×10^{0}	0.00000×10^{0}	6.56356×10^{-5}
Y_O		0.00000×10^{0}	0.00000×10^{0}	8.60924×10^{-4}
Y_{O_2}		2.20149×10^{-1}	2.20149×10^{-1}	1.47849×10^{-2}
Y_{OH}		0.00000×10^{0}	0.00000×10^{0}	6.64695×10^{-3}
Y_{H_2O}		0.00000×10^{0}	0.00000×10^{0}	1.14482×10^{-1}
Y_{HO_2}		0.00000×10^{0}	0.00000×10^{0}	1.13149×10^{-5}
$Y_{H_2O_2}$		0.00000×10^{0}	0.00000×10^{0}	1.27034×10^{-6}
Y_{CH_3}		0.00000×10^{0}	0.00000×10^{0}	5.23100×10^{-14}
Y_{CH_4}		5.51873×10^{-2}	5.51873×10^{-2}	1.53351×10^{-14}
Y_{CO}		0.00000×10^{0}	0.00000×10^{0}	2.36488×10^{-2}
Y_{CO_2}		0.00000×10^{0}	0.00000×10^{0}	1.14235×10^{-1}
Y_{CHO}		0.00000×10^{0}	0.00000×10^{0}	7.22950×10^{-8}
Y_{CH_2O}		0.00000×10^{0}	0.00000×10^{0}	1.43914×10^{-9}
Y_{CH_3O}		0.00000×10^{0}	0.00000×10^{0}	1.88495×10^{-15}
$Y_{C_2H_3}$		0.00000×10^{0}	0.00000×10^{0}	1.38657×10^{-21}
$Y_{C_2H_4}$		0.00000×10^{0}	0.00000×10^{0}	6.00001×10^{-22}
$Y_{C_2H_5}$		0.00000×10^{0}	0.00000×10^{0}	8.53497×10^{-26}
$Y_{C_2H_6}$		0.00000×10^{0}	0.00000×10^{0}	4.26483×10^{-27}
Y_{N_2}		7.24664×10^{-1}	7.24664×10^{-1}	7.24664×10^{-1}
Y_{Ar}		0.00000×10^{0}	0.00000×10^{0}	0.00000×10^{0}

Table 9. Thermochemical and dynamic properties for a mixture of $CH_4 + 2O_2 + 7.52N_2$.

Ref.	Mixture	T_o (K)	p_o (atm)	M_o	ℓ_{ind} (cm) present study	ℓ_{ind} (cm) reported value	ℓ_f (cm)	Δx (cm)
10	$CH_4 + 2O_2 + 7.52N_2$	295	0.503	6.61	3.6×10^{-2}	1.2×10^{-2}	1.8×10^{-6}	1.4×10^{-2} [b]
17	$CH_4 + 2O_2 + 7.52N_2$	295	0.509	6.61	3.8×10^{-2}	1.4×10^{-2}	1.9×10^{-6}	2.1×10^{-4}
18	$9.5CH_4 + 19.0O_2 + 71.5N_2$	295	0.493	6.64	3.7×10^{-2}	$< 1.0 \times 10^{-1}$ [c]	1.9×10^{-6}	2.7×10^{-4} [b]
19	$CH_4 + 2O_2 + 7.52N_2$	295	0.503	6.61	3.6×10^{-2}	1.4×10^{-2}	1.8×10^{-6}	2.8×10^{-4} [b]
20	$CH_4 + 2O_2$	300	0.987	6.71	2.6×10^{-2}	$< 1.0 \times 10^{0}$ [c]	1.2×10^{-5}	- [d]

Table 10. Comparison of length scales among various models which use detailed kinetics to describe detonations in methane-based systems. Values for ℓ_f were predicted from the algorithm of the present study; values for ℓ_{ind} were predicted from the present study and reported from the cited sources. [b]Discretization length not clearly specified; value estimated. [c]Induction length not clearly specified; value estimated. [d]Adaptive grid used; finest resolution not specified.

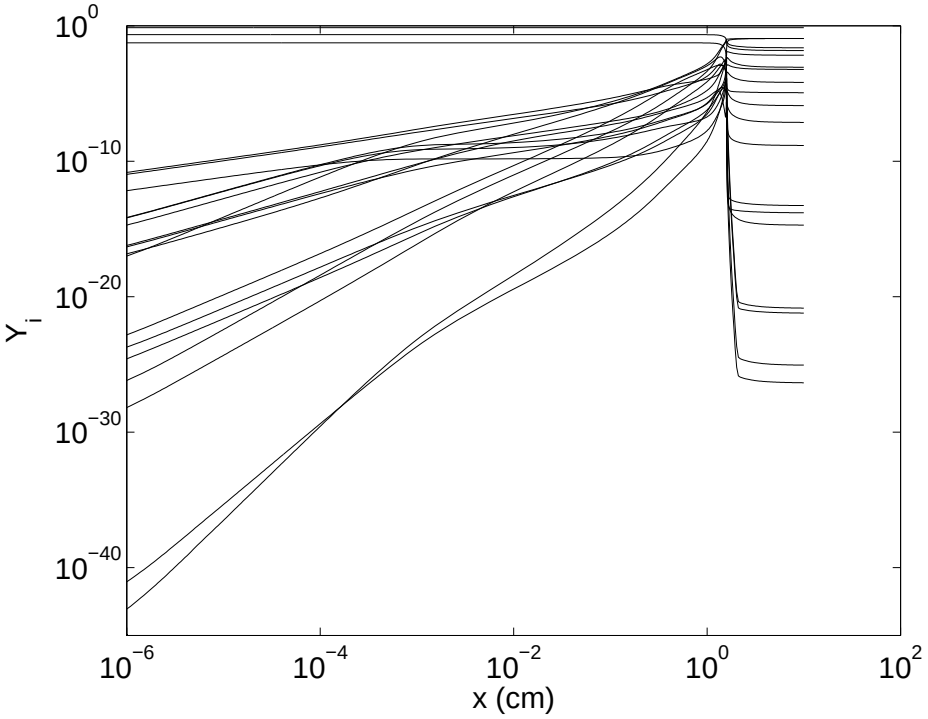

Figure 1. Species mass fraction versus distance for conditions of Table 9.

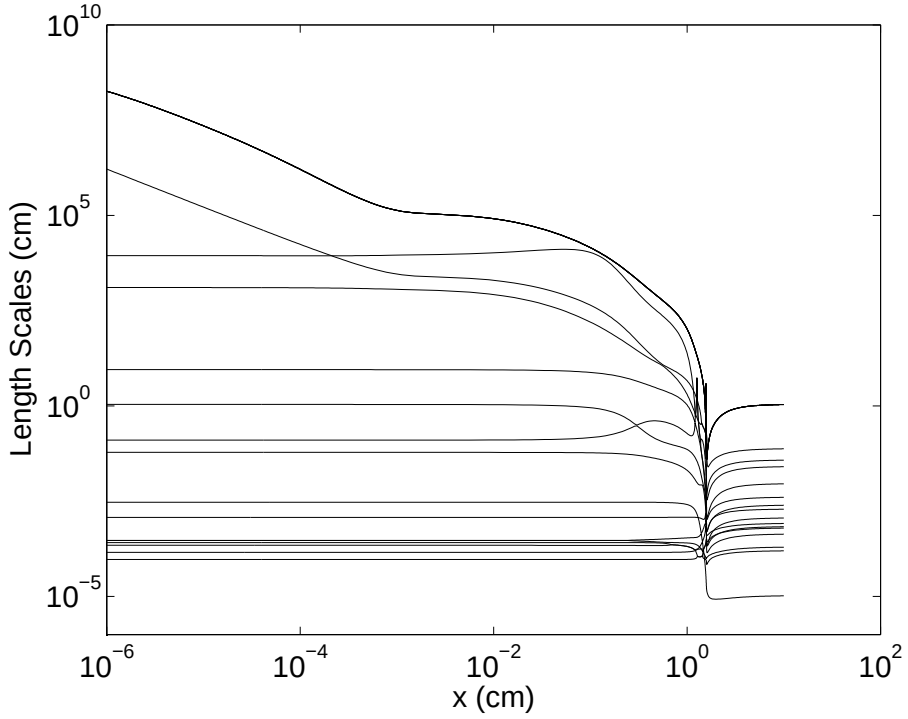

Figure 2. Length scales versus distance for conditions of Table 9.

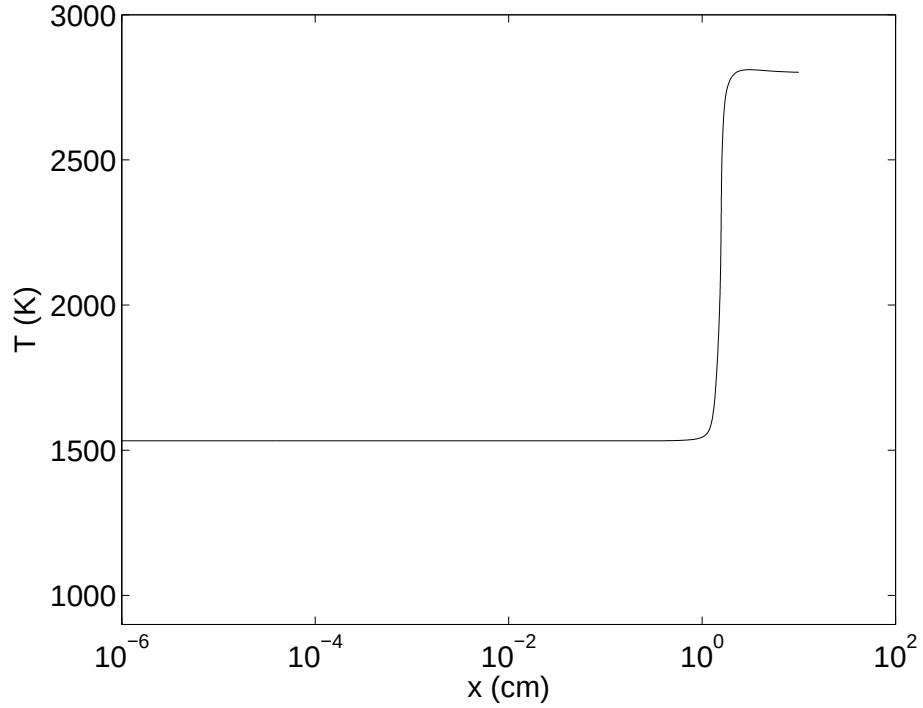

Figure 3. Temperature versus distance for conditions of Table 9.

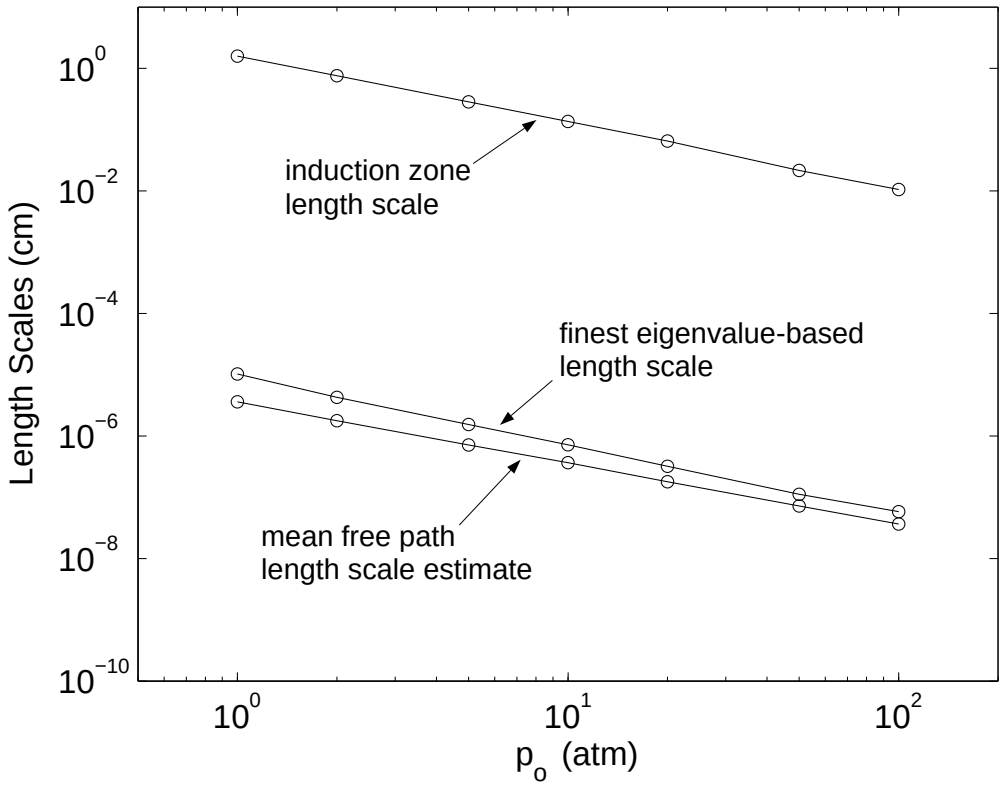

Figure 4. Induction zone length ℓ_{ind}, finest reaction zone length ℓ_f, and mean free path estimate ℓ_{mfp} versus unshocked pressure p_o, with $T_o = 298\ K$ for near-CJ detonation in $CH_4 + 2O_2 + 7.52N_2$.